Switching Behavior of a Heterostructure Based on Periodically Doped Graphene Nanoribbon

Sake Wang[1,*,†] Nguyen T. Hung,[2] Hongyu Tian,[3] Md Shafiqul Islam,[1] and Riichiro Saito[1]

[1]*Department of Physics, Tohoku University, Sendai 980-8578, Japan*

[2]*Frontier Research Institute for Interdisciplinary Sciences, Tohoku University, Sendai 980-8578, Japan*

[3]*School of Physics and Electronic Engineering, Linyi University, Linyi 276005, China*

We theoretically propose a switching device that operates at room temperature. The device is an in-plane heterostructure based on a periodically boron-doped (nitrogen-doped) armchair graphene nanoribbon, which has been experimentally fabricated recently. The calculated *I-V* curve shows that for a realistic device with interface width longer than 20 nm, nonzero electric current occurs only in the region of bias voltage between -0.22 and 0.28 V, which is beneficial to low-voltage operation. Furthermore, in this case, the electric current is robust against the change of the potential profile in the interface since the metallic impurity-induced sub-bands with delocalized wave functions contribute to the transmission exclusively. This also suggests the high response speed of the proposed device. We also discuss the temperature dependence, the output impedance, the effect of phonons, and the possible regimes to extend our work, which suggest that our model may have potential room-temperature nanoelectronics applications.

I. INTRODUCTION

Modern electronic devices are used practically everywhere in our daily lives. Among them, the most fundamental devices are control circuit elements—switching devices. The fabrication of switching devices enjoys remarkable achievements due to Moore's law, together with Dennard's scaling [1,2], which features the higher switching speed with lower voltage [3]. However, around 2006, the voltage could not be lowered further because a fundamental physical limit had been reached [4,5] and hinders further enhancement of speed. This marks a breakdown of Dennard's rule [6]. Nowadays, researchers are continuing their investigations on shrinking the devices, but the fundamental physical limitation still exists. To overcome this difficulty, researchers have proposed many solutions, such as spintronics devices [7–11]. However, the operation speed of spin-based devices is fundamentally limited by the spin-precession time, which is longer than 10–100 ps [12], while the switching speed of the charge-based device can be as short as a few ps [13,14]. Further, at room temperature, thermal fluctuations will act as a random magnetic field that will increase the spin-switching error probability [15,16]. Recently, a topological switching device has been fabricated based on Na_3Bi [17], but

the extreme air sensitivity and difficulties in the fabrication of mesoscopic ultrathin Na_3Bi hinder the utilization of topological switches [18]. Therefore, finding a switching device [19], which provides high-speed, low-voltage, and room-temperature operation is crucial to the continuing flourishing of the industry.

Graphene nanoribbon (GNR) is a one-dimensional (1D) graphene nanostructure whose electronic property depends on edge geometry, ribbon width, chemical doping, and crystallographic symmetry [20–28]. According to the edge geometry, there are two categories of GNRs, namely, armchair GNRs (AGNRs) and zigzag GNRs (ZGNRs). The energy band gap of AGNR oscillates as the number of dimer lines N_a across the ribbon width takes the values of $3p$, $3p + 1$, and $3p + 2$ (p is an integer) families [29]. For a given family of N_a, the energy band gap is inversely proportional to the width [30–34]. We designate AGNR (ZGNR) with N_a dimer lines (N_z zigzag chains) as an N_a-AGNR (N_z-ZGNR) [30]. Because of the gap tunability as a function of N_a, the AGNRs are considered beneficial for electronic device applications [21,35,36]. However, the energy band gaps of AGNRs are sensitive to the chemical doping and doping position in the GNR [22–24]. Depending on the doping position, AGNRs can be either metallic or semiconducting. Among several doping positions in a given AGNR, it was found that doping at the center of the ribbon gives the minimum effect on the electronic structure [37,38]. Further, the high mobility of graphene could be retained by periodically doping rather than randomly

---

*sake@flex.phys.tohoku.ac.jp

†Permanent address: College of Science, Jinling Institute of Technology, Nanjing 211169, China.

doping, especially for the 1D case. Such a strong dependence of the electronic structures and mobility on the structure of AGNRs indicates that atomic precision for the doping in GNR fabrication is required to characterize their electronic properties [23,36].

A bottom-up approach of substitutional impurity for GNR using a well-defined precursor molecule enables the fabrication of atomically precise doped GNRs [39,40]. Using this technique, Carbonell-Sanromà *et al.* [41] synthesized hybrid 7-AGNR, in which the pairs of boron (B) atoms are randomly doped around the center of the ribbon. Scanning tunneling spectroscopy (STS) shows that the energy gap of the hybrid 7-AGNR is 2.4 eV. Furthermore, Kawai *et al.* [42] synthesized periodically doped 7-AGNR, where the pairs of B atoms are *periodically* distributed at the center of the ribbon. By using STS measurement, they obtained an energy gap of about 2.5 eV, which is comparable to that of randomly doped ribbon [41]. On the other hand, Pawlak and Liu *et al.* have realized periodic and precise substitutions of carbons with nitrogen (N) atoms in GNRs on Ag(111) surface [43]. The above experiments indicate that nowadays the periodic and precise doping of *p*-type and *n*-type can be experimentally achieved. In order to get a high-speed switching device, we need to use the fact that periodical doping is not impurity any more. While the random doping gives rise to the localized states [44–46], we expect that periodic doping will induce delocalized energy sub-bands [47–51], where physical properties are fundamentally different from the conventional *p-n* junction. Although the impurity-induced sub-bands in atomically precise doped GNRs have not been observed in experiment yet, the existence of such sub-bands can be observed by STS or angle-resolved photoemission spectroscopy [52,53] at low temperature, if the sub-bands are occupied by electrons. Recently, the fabrication of in-plane heterostructure based on two-dimensional (2D) materials offers unusual physical properties and possible applications as electronic devices [54]. Therefore, by employing the B- and N-doped AGNRs, we could construct an in-plane heterostructure theoretically, which is useful for designing an integrated circuit.

In this paper, we design an in-plane heterostructure in which the left (right) side is periodically B-doped (N-doped) AGNR. Our primary purpose is to show a unique *I-V* curve, which provides a finite current for a narrow region of bias voltage by using the nonequilibrium Green's function. For this purpose, B- and N-doped 7-AGNRs, which we denote as B-AGNR and N-AGNR, respectively, are the optimized geometries that give a low-voltage *I-V* curve in a reasonable energy gap value, that can be observed by the experiment.

The rest of the paper is organized as follows. In Sec. II, we show the proposed in-plane heterostructure and the method to calculate its *I-V* curve. In Sec. III, we show the calculated results and analyze the dependence of electric

current *I* on the potential profile at the interface. We also discuss the temperature dependence, output impedance, phonon effect, and other possible variations of the proposed device to expand our work. Finally, we give the summary in Sec. IV.

II. MODEL AND METHODS

In Figs. 1(a) and 1(b), we show the unit cells of B-AGNR and N-AGNR. Here, the dopant atoms are periodically put at one of the hexagonal corners at the center of the ribbon width. Each carbon (C) atom at armchair edges of GNRs is passivated by hydrogen atom [55]. Since the atomic numbers of B, C, and N are sufficiently small, we neglect the spin-orbit interaction in B, C, and N atoms. Furthermore, unlike FETs, we do not have the gate voltage but only bias voltage in the discussion, the effect of the substrate may not be significant. Thus, we consider the freestanding structure of AGNR and neglect the substrate effect for simplicity. It is worthwhile to note that the present system is not the conventional FET operation, the current is not controlled by gate voltage, but by bias voltage.

We adopt first-principles calculation with the plane-wave basis to optimize the geometry and to calculate ground-state electronic structures of the AGNRs as implemented in the QUANTUM ESPRESSO (QE) package [56,57]. For the geometry optimization, all structures are relaxed
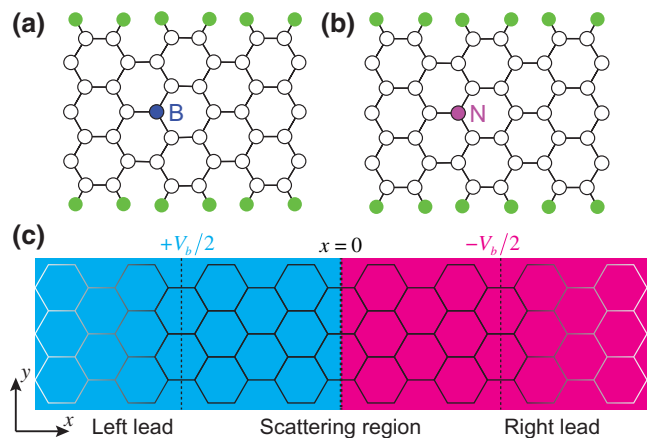

FIG. 1. Unit cells of (a) B-doped and (b) N-doped 7-AGNRs with lattice constants 12.87 and 12.78 Å, respectively. The C atoms are denoted by black open circles while the dopant atoms are denoted by blue (B) and red (N) solid circles. The ribbon edges are passivated by hydrogen atoms (green balls). (c) The in-plane heterostructure, where B-AGNR (N-AGNR) is in the left (right) with blue (red) background. We set the interface as $x = 0$. A bias voltage V_b gives rise to symmetric potential change $\pm V_b/2$ in the left (right) region. The dashed vertical line denotes the boundary between the left, right electrode and scattering region. Fading black in the electrodes indicates continuation to infinity.

until the energy and the force on each atom are less than 10^{-8} Ry and 10^{-4} Ry/a.u., respectively. For the sampling of 1D Brillouin zone, we use $2 \times 1 \times 1$ **k**-point mesh with the Monkhorst–Pack scheme [58], where **k** is the electronic wave vector and the x axis is selected to be the periodic direction of the 1D GNR. For the grid integration, the plane-wave cutoff energy is set to be 80 Ry. To avoid interactions between neighboring ribbons, we maintain the edge-to-edge vacuum distance of 25 Å, and layer-to-layer vacuum distance of 25 Å, which have been checked to be sufficiently large for the present purpose. The Perdew–Burke–Ernzerhof functionals within the generalized gradient approximation are used as the exchange-correlation functionals [59,60]. We also utilize the norm-conserving pseudopotentials [61,62] to treat the electron-ion interaction.

By implementing the QE package [56,57], we can obtain the electronic structures of periodically doped AGNRs. Further, using the results of QE, we adopt Wannier90 [63,64] to find the Hamiltonian matrix element $H_{mn}^{\mathbf{R}}$ in the Wannier-function (WF) basis, which defines the on-site potential and the hopping matrix elements between maximally localized WF (MLWF) m in the unit cell at $\mathbf{r} = \mathbf{0}$ and MLWF n in the unit cell at $\mathbf{r} = \mathbf{R}$. Then we further construct the tight-binding (TB) Hamiltonian matrix as follows [65]:

$$H_{mn}(\mathbf{k}) = \sum_{\mathbf{R}} e^{i\mathbf{k}\cdot\mathbf{R}} H_{mn}^{\mathbf{R}}. \quad (1)$$

We get the energy band $\varepsilon_n(\mathbf{k})$ as eigenvalues of the matrix $H_{mn}(\mathbf{k})$. The DOS and partial DOS (PDOS) are also computed by Wannier90 using $400 \times 10 \times 10$ **k**-point mesh.

In Fig. 1(c), we show an in-plane heterostructure by combining B-AGNR and N-AGNR on the left and right side, respectively. The geometry of the heterostructure consists of a semi-infinite left electrode, a semi-infinite right electrode, and a scattering region. We set the interface at $x = 0$. A bias voltage V_b gives rise to symmetric potential change $V_b/2$ $(-V_b/2)$ in the left (right) region.

Since we employ the MLWF, it offers an ideal tool [66,67] for discussing the I-V curve as a function of bias voltage V_b by the nonequilibrium Green's function [68–79]. The transmission probability of an electron with the energy E from the left electrode to the right electrode is given by

$$T(E, V_b) = \mathrm{tr}\left[\Gamma_L(E, V_b) G^r(E, V_b) \Gamma_R(E, V_b) G^a(E, V_b)\right], \quad (2)$$

where $G^{r,a}(E, V_b)$ is the retarded (r) or advanced (a) Green's function across the heterostructure. The level-width function [69,80] (or the level-width matrix [72]) [81]

$\Gamma_{L,R}(E, V_b)$ is given by

$$\Gamma_{L,R}(E, V_b) = i\left[\Sigma_{L,R}^r(E, V_b) - \Sigma_{L,R}^a(E, V_b)\right], \quad (3)$$

where $\Sigma_{L,R}^r(E, V_b)$ [$\Sigma_{L,R}^a(E, V_b)$] is the retarded [advanced] surface self-energies of the left (L) or right (R) electrodes. $\Sigma_{L,R}^{r,a}(E, V_b)$ is obtained by using an iterative method [82], which is feasible if we consider only the electron hopping up to 12 Å, smaller than the lattice constants of the unit cell for B-AGNR (12.87 Å) and N-AGNR (12.78 Å) derived from the QE calculation. Here we need three sets of TB parameters to express (1) B-AGNR region, (2) N-AGNR region, and (3) interface region, respectively, to further calculate $G^{r,a}(E, V_b)$ in Eq. (2). For (1) and (2), we adopt the energy bands of B-AGNR and N-AGNR, respectively. For (3), we need to consider a large unit cell that combines the unit cells of B-AGNR and N-AGNR for obtaining TB parameters near the interface. Further, as in transport studies [26,74–76,83,84] and impurity doping [85] in graphene, we do not consider the effect of potential change on the modification of hopping matrix elements.

The current I as a function of V_b, or the I-V curve, can be calculated by the Landauer–Büttiker formula [86–92]

$$I(V_b) = \frac{2e}{h} \int_{-\infty}^{\infty} T(E, V_b) \left[f_L(E, V_b) - f_R(E, V_b)\right] dE, \quad (4)$$

where e is the elementary charge and h is the Planck constant. The factor 2 is the spin degeneracy. $f_{L,R}(E, V_b)$ is the Fermi–Dirac distribution function for the left or right electrodes. In Eq. (4) we consider the fact that the electrochemical potential $\mu_{L,R}$ in $f_{L,R}(E, V_b)$ can be shifted by the bias voltage V_b. In fact, at 0 K, $f_L(E, V_b)$ and $f_R(E, V_b)$ are step functions of E and have a value of the unity when E is below $\mu_L(V_b) = E_F + eV_b/2$ and $\mu_R(V_b) = E_F - eV_b/2$, respectively. Otherwise, the $f_{L,R}(E, V_b)$ is zero. Therefore, the integral of Eq. (4) becomes $\int_{-eV_b/2}^{eV_b/2} T(E, V_b) dE$ for 0 K and the energy interval $[-eV_b/2, eV_b/2]$ is called the bias window [93].

III. RESULTS AND DISCUSSION

In Fig. 2(a), we show the calculated band structure of undoped 7-AGNR, which reproduces the previous work [94]. In Figs. 2(b) and 2(d), we show the calculated energy band structures of B-AGNR and N-AGNR with the corresponding plots for DOS in Figs. 2(c) and 2(e), respectively. We can see that the Wannier interpolated TB band structure [red × symbols in Figs. 2(b) and 2(d)] from Eq. (1) reproduces the density-functional-theory (DFT) calculation performed by QE (solid black lines) well. It is worth noting that the B and N atomic orbitals (blue and red lines) do not contribute much to the DOS of sub-bands [48] as shown as PDOS in Figs. 2(c) and 2(e). We multiply the
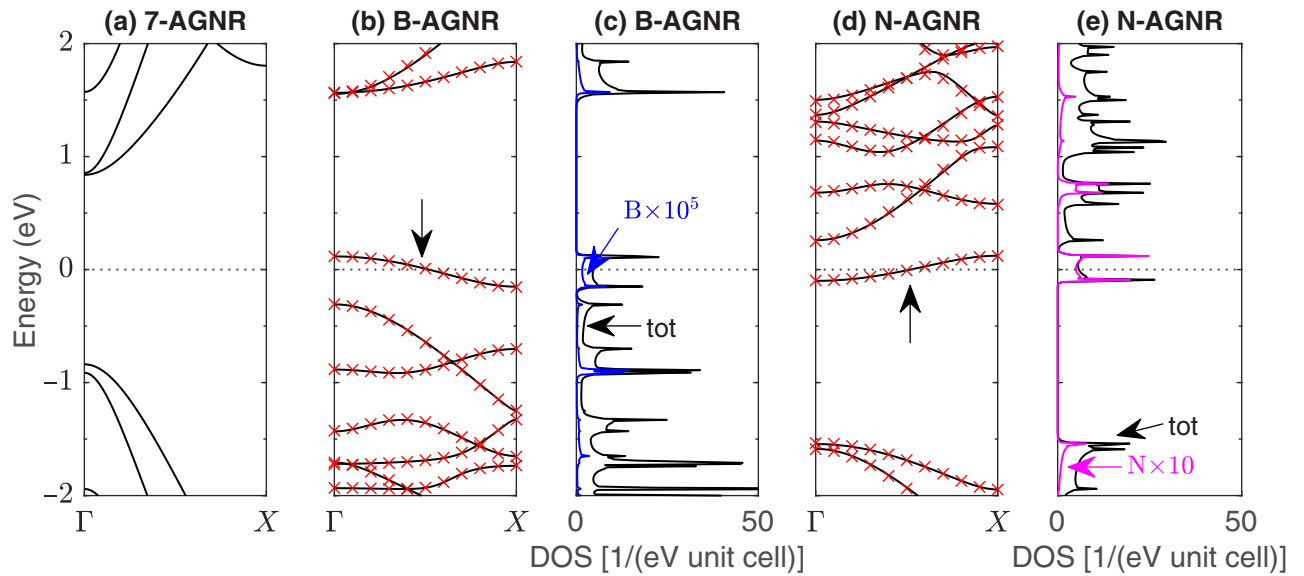
FIG. 2.   Calculated energy band structures of (a) undoped 7-AGNR, (b) B-AGNR, and (d) N-AGNR from DFT calculations (solid black lines) and via Wannier interpolated tight-binding model (red × symbols) with the corresponding plots for density of states (DOS) for (b) and (d) in (c) and (e), respectively. The Fermi energy is indicated by the horizontal dotted line and crosses the impurity-induced sub-band, which is pointed out by arrows in (b) and (d). It is noted that we multiply the partial DOS of B and N by 10^5 and 10, respectively.

PDOS of B and N by 10^5 and 10, respectively, in the plot. Therefore, we can conclude that all the sub-bands are made by π orbitals of carbon atoms [95].

We can see that in addition to the band structure of undoped 7-AGNR, the B-AGNR (N-AGNR) introduces a new cosinelike sub-band above (below) the valence (conductance) bands at the Fermi energy $E = 0$, which is pointed out by the arrow and ranges $[-0.16, 0.12]$ ($[-0.10, 0.12]$) eV. As the Fermi energy crosses the center of the impurity-induced sub-band, there are unoccupied states above the Fermi level in the sub-band. Thus, for the electron conduction with the common Fermi level, the electrons in the induced sub-band do not require any thermal excitation and thus behaves as a metal. The group velocity of electrons at the Fermi energy of B-AGNR and N-AGNR is approximately 2.3×10^5 m/s, smaller than graphene (approximately 10^6 m/s [96]), which still gives a high-speed response compared with conventional impurity levels.

In a practical device with impurity levels, when the heterostructure is formed, the width of the depletion region depends on many parameters [97,98], such as doping concentration, temperature, dielectric constant, etc. [47,99]. For simplicity, we express the potential by the smoothstep function [83,100] with a parameter ℓ,

$$V(x) = \frac{V_b}{2} \tanh\left(-\frac{2x}{\ell}\right). \tag{5}$$

As shown in the inset of Fig. 3, the potential $V(x)$ monotonically decreases from $V_b/2$ to $-V_b/2$ over a distance (width) ℓ around the interface ($x = 0$) for $V_b > 0$ [100]. We show that the result does not depend on ℓ and thus we can safely neglect the effect of the environment on ℓ.
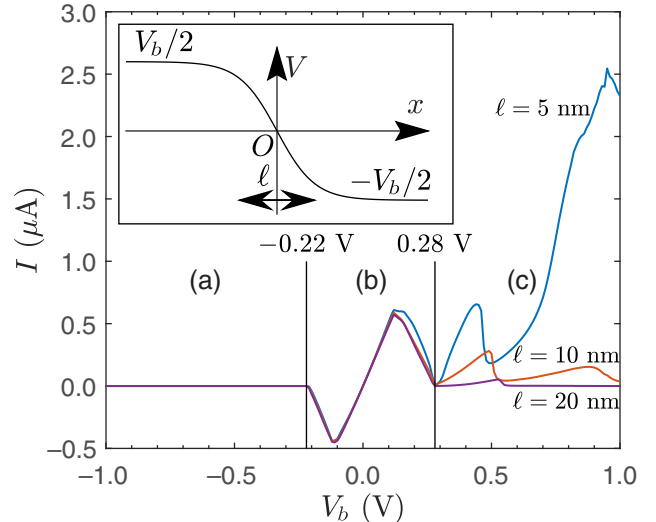

FIG. 3.   (Inset) Potential profile of the interface represented by the smoothstep function $V(x) = (V_b/2) \tanh (-2x/\ell)$, here the potential $V(x)$ decreases from $V_b/2$ to $-V_b/2$ over a distance ℓ around $x = 0$ if $V_b > 0$. (Main panel) The corresponding I-V curve with various ℓ. The regions labeled (a)–(c) indicate the three cases of I-V curve discussed in the main text.

In Fig. 3, we plot the calculated I-V curves for $\ell = 5$, 10, and 20 nm. We can see that the trend of the I-V curve is almost the same for different ℓ's except for $V_b > 0.28$ V and we can categorize the results into three cases: (a) $V_b < -0.22$ V, (b) -0.22 V $< V_b < 0.28$ V, and (c) $V_b > 0.28$ V.

For (a) $V_b < -0.22$ V, as we discuss in Eq. (4), the band structures of the two electrodes shift vertically as we change the bias voltage V_b. When we decrease $V_b < 0$, the Fermi level of the left (right) electrode gradually decreases (increases). After we further decrease V_b from the critical point that the top of the impurity-induced sub-band of B-AGNR aligns with the bottom of the impurity-induced sub-band of N-AGNR. This corresponds to $eV_b = -0.10 - 0.12 = -0.22$ eV. Therefore, the states in the left and right electrodes no longer overlap in the bias window when $V_b < -0.22$ V. As a result, for any energy in the bias window, electrons could not transmit. This leads to zero current for all ℓ's.

For (b) -0.22 V $< V_b < 0.28$ V, the current I is robust against the change of ℓ. In Fig. 4(a), we show the band structures of left and right electrodes with the corresponding transmission for $V_b = 0.1$ V, the impurity-induced sub-bands contribute to the transmission probability since the bias window contains only the two impurity-induced sub-bands. Since the wave function of impurity-induced sub-bands is delocalized, from the B-doped side to the N-doped side, and the I-V characteristic does not depend on ℓ. It is consistent with our results of projected DOS shown in Figs. 2(b) and 2(d), in which the calculated PDOS of B (N) atoms is small compared with the total DOS of B-AGNR (N-AGNR). This indicates that the current flows over the sample.

The shape of the I-V curve in case (b) can be explained as follows. When $|V_b|$ increases from zero, the current initially increases with increasing bias window. However, after further increase of $|V_b|$, the overlapping energy region of impurity-induced sub-bands from both electrodes decreases, which leads to the decrease of I. This indicates negative resistance region, which is similar to the Esaki diode [101], though the Esaki diode has the finite current only for $V_b > 0$. The current drops to zero at the critical point that the top (bottom) of the impurity-induced sub-band of B-AGNR aligns with the bottom (top) of the impurity-induced sub-band of N-AGNR for $V_b < 0$ ($V_b > 0$). This corresponds to $eV_b = -0.22$ eV for $V_b < 0$ as discussed in case (a) and $eV_b = 0.12 - (-0.16) = 0.28$ eV for $V_b > 0$. Therefore, the two impurity-induced sub-bands are completely misaligned when $V_b < -0.22$ V or $V_b > 0.28$ V. Considering the delocalized wave function of electrons in the impurity-induced sub-bands, we expect a high-speed response of our suggested device.

For case (c), when V_b is larger than 0.28 V, the current reappears since the impurity-induced sub-band from the B-doped (N-doped) side begins to overlap with the
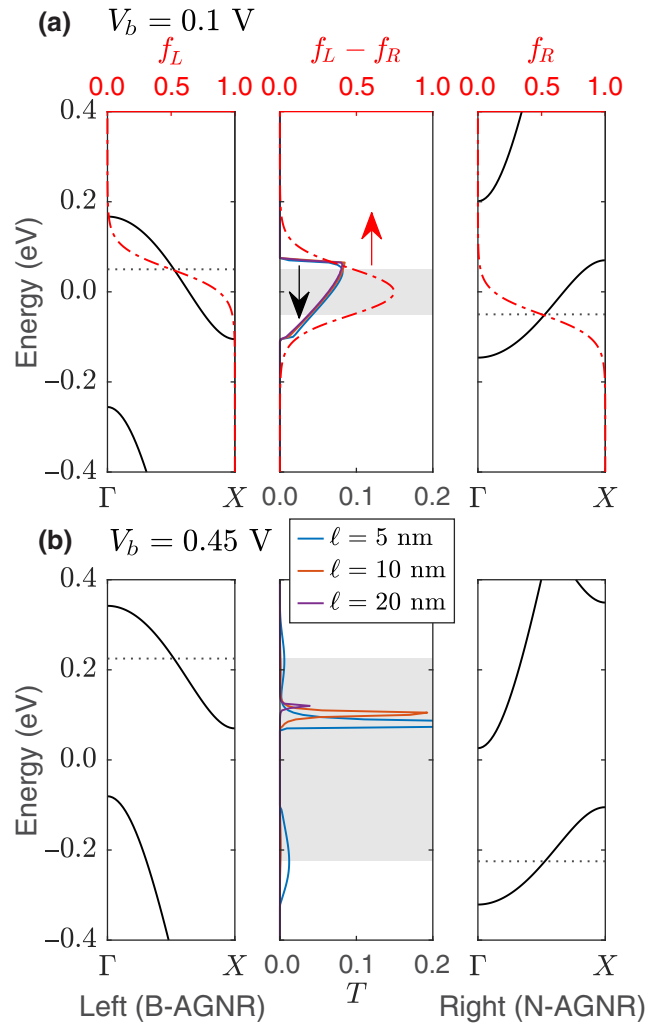

FIG. 4. Band structures of both left and right electrodes with transmission probability in the middle for $\ell = 5$, 10, and 20 nm at (a) $V_b = 0.1$ and (b) 0.45 V. The dotted lines indicate the electrochemical potentials of the electrodes and give the bias window (shaded area) in the middle figure. In (a), Fermi–Dirac distribution function $f_{L,R}(E, V_b)$ versus energy at room temperature (300 K) is also plotted in red dash-dotted line for each electrode with respect to the top x axes.

conduction (valence) bands from the other side. Basically, the current I increases when V_b increases because of a larger bias window. However, I reaches to a local maximum when $V_b \approx 0.45$ V. We plot the band structures and transmission at $V_b = 0.45$ V as shown in Fig. 4(b). The two gaps between the impurity-induced sub-band and the valence (conduction) bands in the B-doped (N-doped) region align with each other. It is noted that after further increase of V_b, the two gaps suffer misalignment and restrict the transmission in a wider energy range, causing a drop of current at around $V_b = 0.5$ V as shown in Fig. 3. As we can see in Fig. 4(b), the peak of transmission probability at around $V_b = 0.5$ V shifts to larger energy when ℓ

increases. This could explain the peak near 0.5 V in Fig. 3 moves to the right when ℓ increases.

It is also essential to understand the ℓ dependence of the current for $V_b > 0.28$ V. We can see that the current quickly decreases with increasing ℓ for $V_b > 0.28$ V. For $\ell = 20$ nm, I almost drops to zero in this region. This is consistent with Fig. 4(b) in which transmission probability T decreases when ℓ increases. The reason of a smaller T for a larger ℓ is that for a smoother potential profile, electrons suffer backscattering when they approach the interface and the conductance becomes smaller by approximately a factor of $\sqrt{k_F \ell}$ compared to sharp ones, where k_F is the Fermi wave vector [91,102–104]. Here we need to note that in this heterostructure, the scattering process is much more complicated. Similar results are found in the pristine graphene applied with bias voltage, which induces smooth potential profile [76]. Therefore, since the nonzero T survives only in the energy range of less than 0.1 eV for $\ell = 5$ nm, we can conclude that the electric current in this case is almost zero as shown in Fig. 3 for $\ell > 20$ nm.

In real 2D in-plane heterostructures with bias voltage, ℓ is often in the order of 0.1 μm [105–108], much larger than 20 nm and it can be measured directly by the Seebeck coefficient or the thermoelectric power [109]. Therefore, in experiment, the *I-V* curve should be similar to the situation of $\ell = 20$ nm, in which the current exists only in the region of case (b) -0.22 V $< V_b < 0.28$ V. Further, in Fig. 4(a), we also plot the Fermi–Dirac distribution function $f_{L,R}(E, V_b)$ versus energy at room temperature (300 K) in red dash-dotted line for each electrode with respect to the top x axes. We can see that the Fermi–Dirac distribution function affects only the impurity-induced sub-bands. Therefore, the robustness of I on ℓ when -0.22 V $< V_b < 0.28$ V still survive even at room temperature.

We estimate the output impedance [110] $Z = V_b/I$ of the present model. We consider only the current contributed by the impurity-induced sub-bands (-0.22 V $< V_b < 0.28$ V), and the corresponding output impedance is approximately 200 kΩ. Since the typical impedance value for a transistor is 100 kΩ [111], it suggests that the present device could be used in the electric circuit. We can imagine a switching device that operates at both sides of the bias voltage. Although triac [112] can behave as a semiconductor switch in both positive and negative voltages with breakover voltage, the present device allows electric current only in a finite bias range, between -0.22 and 0.28 V. Further, we can make an oscillating device using the bias-voltage region with using negative resistance [113].

Here we briefly discuss the effects of phonons at nonzero temperature. The dominant electron–phonon interaction in graphene is the optical phonon with energy approximating to 0.2 eV [114,115]. However, our proposed device operates in the range of -0.22 to 0.28 V. Therefore, the electron–phonon interaction for optical phonon will not affect the *I-V* curve within the range of -0.2 V $< V_b <$

0.2 V, which is a large portion in the operating range of the proposed device. This is an advantage of our device. The other part is the electron–acoustic phonon interactions [115], an electron emits or absorbs acoustic phonon by electron–phonon interaction, which leads to increased resistance of graphene. However, at room temperature, the intrinsic resistivity of graphene by acoustic phonons would be sufficiently small such as 30 Ω [116], which can be neglected compared with the calculated impedance 200 kΩ.

At last, we would like to extend our work by demonstrating the feasibility of the proposed device for other geometries and variations of the GNRs. Considering the number of widths [20] and the sensitivity of band structures to doping sites in GNRs [24], we would like to give some qualitative discussions since we cannot do the DFT calculations for all widths and geometries. For AGNRs in a given family of N_a, the energy band gap is inversely proportional to the width of AGNR. Therefore, the width of the impurity-induced sub-band will decrease with increasing N_a. This will further shrink the operation range (smaller range of V_b for nonzero I) in our proposed device. For variations of edge terminations, since the doping site is far from the edge, the modification to the impurity-induced sub-bands can be neglected in the first approximation. Here we also include some previous DFT studies for designing the device, which report the metallic sub-bands in doped GNRs. Such as B-doped (N-doped) 8-AGNR [48], selective B-doping of 12- and 16-AGNRs [49], both B- and N-doped 6-AGNR [50] and 4-ZGNR [51], etc. [117,118].

IV. SUMMARY

We theoretically investigate the electronic transport properties of an in-plane heterostructure in which the left (right) side is based on B-AGNR (N-AGNR). If we adopt a realistic device with interface width in the order of 0.1 μm, nonzero electric current occurs only when -0.22 V $< V_b < 0.28$ V. Furthermore, in this case, the electric current is robust against the change of the potential profile since the impurity-induced sub-bands with delocalized wave functions contribute to the transmission exclusively. Our results suggest that our model may have potential room-temperature nanoelectronics applications if it is fabricated.

———————

[1] R. H. Dennard, F. H. Gaensslen, H. Yu, V. L. Rideout, E. Bassous, and A. R. LeBlanc, Design of ion-implanted MOSFET's with very small physical dimensions, IEEE J. Solid-State Circuits **9**, 256 (1974).

[2] G. Baccarani, M. R. Wordeman, and R. H. Dennard, Generalized scaling theory and its application to a ¼ micrometer MOSFET design, IEEE Trans. Electron Devices **31**, 452 (1984).

[3] B. G. Streetman and S. K. Banerjee, *Solid State Electronic Devices* (Pearson, Upper Saddle River, 2015).

[4] D. M. Newns, B. G. Elmegreen, X.-H. Liu, and G. J. Martyna, The piezoelectronic transistor: A nanoactuator-based post-CMOS digital switch with high speed and low power, MRS Bull. **37**, 1071 (2012).

[5] M. Bohr, A 30 year retrospective on Dennard's MOSFET scaling paper, IEEE SSCS Newsletter **12**, 11 (2007).

[6] W. Haensch, E. J. Nowak, R. H. Dennard, P. M. Solomon, A. Bryant, O. H. Dokumaci, A. Kumar, X. Wang, J. B. Johnson, and M. V. Fischetti, Silicon CMOS devices beyond scaling, IBM J. Res. Dev. **50**, 339 (2006).

[7] M. N. Baibich, J. M. Broto, A. Fert, F. Nguyen Van Dau, F. Petroff, P. Etienne, G. Creuzet, A. Friederich, and J. Chazelas, Giant Magnetoresistance of (001)Fe/(001)Cr Magnetic Superlattices, Phys. Rev. Lett. **61**, 2472 (1988).

[8] G. Binasch, P. Grünberg, F. Saurenbach, and W. Zinn, Enhanced magnetoresistance in layered magnetic structures with antiferromagnetic interlayer exchange, Phys. Rev. B **39**, 4828 (1989).

[9] S. A. Wolf, D. D. Awschalom, R. A. Buhrman, J. M. Daughton, S. von Molnár, M. L. Roukes, A. Y. Chtchelkanova, and D. M. Treger, Spintronics: A spin-based electronics vision for the future, Science **294**, 1488 (2001).

[10] I. Žutić, J. Fabian, and S. Das Sarma, Spintronics: Fundamentals and applications, Rev. Mod. Phys. **76**, 323 (2004).

[11] X. Lin, W. Yang, K. L. Wang, and W. Zhao, Two-dimensional spintronics for low-power electronics, Nat. Electron. **2**, 274 (2019).

[12] J.-Y. Chen, L. He, J.-P. Wang, and M. Li, All-Optical Switching of Magnetic Tunnel Junctions with Single Sub-picosecond Laser Pulses, Phys. Rev. Appl. **7**, 021001 (2017).

[13] M. S. Nikoo, A. Jafari, R. van Erp, and E. Matioli, Kilowatt-range picosecond switching based on microplasma devices, IEEE Electron Device Lett. **42**, 767 (2021).

[14] M. S. Nikoo, A. Jafari, N. Perera, M. Zhu, G. Santoruvo, and E. Matioli, Nanoplasma-enabled picosecond switches for ultrafast electronics, Nature **579**, 534 (2020).

[15] M. Salehi Fashami, J. Atulasimha, and S. Bandyopadhyay, Magnetization dynamics, throughput and energy dissipation in a universal multiferroic nanomagnetic logic gate with fan-in and fan-out, Nanotechnology **23**, 105201 (2012).

[16] A. D. Kent and D. C. Worledge, A new spin on magnetic memories, Nat. Nanotechnol. **10**, 187 (2015).

[17] J. L. Collins, A. Tadich, W. Wu, L. C. Gomes, J. N. B. Rodrigues, C. Liu, J. Hellerstedt, H. Ryu, S. Tang, S.-K. Mo, S. Adam, S. A. Yang, M. S. Fuhrer, and M. T. Edmonds, Electric-field-tuned topological phase transition in ultrathin Na_3Bi, Nature **564**, 390 (2018).

[18] I. Di Bernardo, J. Hellerstedt, C. Liu, G. Akhgar, W. Wu, S. A. Yang, D. Culcer, S.-K. Mo, S. Adam, M. T. Edmonds, and M. S. Fuhrer, Progress in epitaxial thin-film Na_3Bi as a topological electronic material, Adv. Mater. **33**, 2005897 (2021).

[19] T. N. Theis and P. M. Solomon, It's time to reinvent the transistor!, Science **327**, 1600 (2010).

[20] X.-L. Wei, H. Fang, R.-Z. Wang, Y.-P. Chen, and J.-X. Zhong, Energy gaps in nitrogen delta-doping graphene: A first-principles study, Appl. Phys. Lett. **99**, 012107 (2011).

[21] Y.-C. Chen, D. G. de Oteyza, Z. Pedramrazi, C. Chen, F. R. Fischer, and M. F. Crommie, Tuning the band gap of graphene nanoribbons synthesized from molecular precursors, ACS Nano **7**, 6123 (2013).

[22] J. Liu, Z. H. Zhang, X. Q. Deng, Z. Q. Fan, and G. P. Tang, Electronic structures and transport properties of armchair graphene nanoribbons by ordered doping, Org. Electron. **18**, 135 (2015).

[23] H. Jippo and M. Ohfuchi, First-principles study of edge-modified armchair graphene nanoribbons, J. Appl. Phys. **113**, 183715 (2013).

[24] C. Shao, C. Rui, J. Liu, T. Wang, Q. Shao, and F. Chen, A first-principles study of fluoride saturation effect on the electronic transport properties of boron-doping armchair graphene nanoribbons, Diam. Relat. Mater. **106**, 107824 (2020).

[25] S. K. Wang and J. Wang, Valley precession in graphene superlattices, Phys. Rev. B **92**, 075419 (2015).

[26] A. Rycerz, J. Tworzydło, and C. W. J. Beenakker, Valley filter and valley valve in graphene, Nat. Phys. **3**, 172 (2007).

[27] S. Wang and J. Yu, Bandgap modulation of partially chlorinated graphene (C_4Cl) nanosheets via biaxial strain and external electric field: a computational study, Appl. Phys. A **124**, 487 (2018).

[28] S. Wang and J. Yu, Magnetic behaviors of 3d transition metal-doped silicane: a first-principle study, J. Supercond. Nov. Magn. **31**, 2789 (2018).

[29] M. V. Fischetti, J. Kim, S. Narayanan, Z.-Y. Ong, C. Sachs, D. K. Ferry, and S. J. Aboud, Pseudopotential-based studies of electron transport in graphene and graphene nanoribbons, J. Phys.: Condens. Matter **25**, 473202 (2013).

[30] Y.-W. Son, M. L. Cohen, and S. G. Louie, Energy gaps in graphene nanoribbons, Phys. Rev. Lett. **97**, 216803 (2006).

[31] Y.-W. Son, M. L. Cohen, and S. G. Louie, Erratum: Energy gaps in graphene nanoribbons [Phys. Rev. Lett. **97**, 216803 (2006)], Phys. Rev. Lett. **98**, 089901(E) (2007).

[32] A. Kimouche, M. M. Ervasti, R. Drost, S. Halonen, A. Harju, P. M. Joensuu, J. Sainio, and P. Liljeroth, Ultranarrow metallic armchair graphene nanoribbons, Nat. Commun. **6,** 10177 (2015).

[33] O. Deniz, C. Sánchez-Sánchez, T. Dumslaff, X. Feng, A. Narita, K. Müllen, N. Kharche, V. Meunier, R. Fasel, and P. Ruffieux, Revealing the electronic structure of silicon intercalated armchair graphene nanoribbons by scanning tunneling spectroscopy, Nano Lett. **17,** 2197 (2017).

[34] N. Merino-Díez, A. Garcia-Lekue, E. Carbonell-Sanromà, J. Li, M. Corso, L. Colazzo, F. Sedona, D. Sánchez-Portal, J. I. Pascual, and D. G. de Oteyza, Width-dependent band gap in armchair graphene nanoribbons reveals Fermi level pinning on Au(111), ACS Nano **11,** 11661 (2017).

[35] W.-X. Wang, M. Zhou, X. Li, S.-Y. Li, X. Wu, W. Duan, and L. He, Energy gaps of atomically precise armchair graphene sidewall nanoribbons, Phys. Rev. B **93,** 241403(R) (2016).

[36] P. Ruffieux, J. Cai, N. C. Plumb, L. Patthey, D. Prezzi, A. Ferretti, E. Molinari, X. Feng, K. Müllen, C. A. Pignedoli, and R. Fasel, Electronic structure of atomically precise graphene nanoribbons, ACS Nano **6,** 6930 (2012).

[37] B. Biel, X. Blase, F. Triozon, and S. Roche, Anomalous doping effects on charge transport in graphene nanoribbons, Phys. Rev. Lett. **102,** 096803 (2009).

[38] R. R. Cloke, T. Marangoni, G. D. Nguyen, T. Joshi, D. J. Rizzo, C. Bronner, T. Cao, S. G. Louie, M. F. Crommie, and F. R. Fischer, Site-specific substitutional boron doping of semiconducting armchair graphene nanoribbons, J. Am. Chem. Soc. **137,** 8872 (2015).

[39] J. Cai, P. Ruffieux, R. Jaafar, M. Bieri, T. Braun, S. Blankenburg, M. Muoth, A. P. Seitsonen, M. Saleh, X. Feng, K. Müllen, and R. Fasel, Atomically precise bottom-up fabrication of graphene nanoribbons, Nature **466,** 470 (2010).

[40] T. Niu, J. Zhang, and W. Chen, Surface engineering of two-dimensional materials, ChemNanoMat **5,** 6 (2019).

[41] E. Carbonell-Sanromà, P. Brandimarte, R. Balog, M. Corso, S. Kawai, A. Garcia-Lekue, S. Saito, S. Yamaguchi, E. Meyer, D. Sánchez-Portal, and J. I. Pascual, Quantum dots embedded in graphene nanoribbons by chemical substitution, Nano Lett. **17,** 50 (2017).

[42] S. Kawai, S. Saito, S. Osumi, S. Yamaguchi, A. S. Foster, P. Spijker, and E. Meyer, Atomically controlled substitutional boron-doping of graphene nanoribbons, Nat. Commun. **6,** 8098 (2015).

[43] R. Pawlak, X. Liu, S. Ninova, P. D'Astolfo, C. Drechsel, S. Sangtarash, R. Häner, S. Decurtins, H. Sadeghi, C. J. Lambert, U. Aschauer, S.-X. Liu, and E. Meyer, Bottom-up synthesis of nitrogen-doped porous graphene nanoribbons, J. Am. Chem. Soc. **142,** 12568 (2020).

[44] W. P. Su, Effect of random doping on the electronic spectrum in trans-polyacetylene, Solid State Commun. **47,** 947 (1983).

[45] C. Özdoğan, J. Kunstmann, and A. Quandt, Localization of metallicity and magnetic properties of graphene and of graphene nanoribbons doped with boron clusters, Philos. Mag. **94,** 1841 (2014).

[46] K. Seeger, *Semiconductor Physics: An Introduction*, Advanced Texts in Physics (Springer, Berlin, 2004).

[47] C. G. Fonstad, *Microelectronic Devices and Circuits* (McGraw-Hill Education, New York, 1994).

[48] S. S. Yu, W. T. Zheng, and Q. Jiang, Electronic properties of nitrogen-/boron-doped graphene nanoribbons with armchair edges, IEEE Trans. Nanotechnol. **9,** 78 (2010).

[49] P. Navarro-Santos, J. L. Ricardo-Chávez, M. Reyes-Reyes, J. L. Rivera, and R. López-Sandoval, Tuning the electronic properties of armchair carbon nanoribbons by a selective boron doping, J. Phys.: Condens. Matter **22,** 505302 (2010).

[50] N. Alaal, N. Medhekar, and A. Shukla, Tunable electronic properties of partially edge-hydrogenated armchair boron–nitrogen–carbon nanoribbons, Phys. Chem. Chem. Phys. **20,** 10345 (2018).

[51] T. Guerra, L. R. S. Araújo, and S. Azevedo, Graphene and boron nitride nanoribbons with multiple doping: an ab initio study, Eur. Phys. J. B **94,** 67 (2021).

[52] C.-Y. Lin, R.-B. Chen, Y.-H. Ho, and M.-F. Lin, *Electronic and Optical Properties of Graphite-Related Systems* (CRC Press, Boca Raton, 2017).

[53] L. F. J. Piper, L. Colakerol, P. D. C. King, A. Schleife, J. Zúñiga-Pérez, P.-A. Glans, T. Learmonth, A. Federov, T. D. Veal, F. Fuchs, V. Muñoz-Sanjosé, F. Bechstedt, C. F. McConville, and K. E. Smith, Observation of quantized subband states and evidence for surface electron accumulation in CdO from angle-resolved photoemission spectroscopy, Phys. Rev. B **78,** 165127 (2008).

[54] A. Di Bartolomeo, Emerging 2D materials and their van der Waals heterostructures, Nanomaterials **10,** 579 (2020).

[55] G. Wang, Effect of edge-hydrogen passivation and saturation on the carrier mobility of armchair graphene nanoribbons, Chem. Phys. Lett. **533,** 74 (2012).

[56] P. Giannozzi *et al.*, QUANTUM ESPRESSO: a modular and open-source software project for quantum simulations of materials, J. Phys.: Condens. Matter **21,** 395502 (2009).

[57] P. Giannozzi *et al.*, Advanced capabilities for materials modelling with Quantum ESPRESSO, J. Phys.: Condens. Matter **29,** 465901 (2017).

[58] H. J. Monkhorst and J. D. Pack, Special points for Brillouin-zone integrations, Phys. Rev. B **13,** 5188 (1976).

[59] J. P. Perdew, K. Burke, and M. Ernzerhof, Generalized gradient approximation made simple, Phys. Rev. Lett. **77,** 3865 (1996).

[60] J. P. Perdew, K. Burke, and M. Ernzerhof, Erratum: Generalized gradient approximation made simple [Phys. Rev. Lett. **77,** 3865 (1996)], Phys. Rev. Lett. **78,** 1396(E) (1997).

[61] N. Troullier and J. L. Martins, Efficient pseudopotentials for plane-wave calculations, Phys. Rev. B **43,** 1993 (1991).

[62] I. Morrison, D. M. Bylander, and L. Kleinman, Nonlocal Hermitian norm-conserving Vanderbilt pseudopotential, Phys. Rev. B **47,** 6728 (1993).

[63] A. A. Mostofi, J. R. Yates, G. Pizzi, Y.-S. Lee, I. Souza, D. Vanderbilt, and N. Marzari, An updated version of wannier90: A tool for obtaining maximally-localised Wannier functions, Comput. Phys. Commun. **185,** 2309 (2014).

[64] G. Pizzi *et al.,* Wannier90 as a community code: new features and applications, J. Phys.: Condens. Matter **32,** 165902 (2020).

[65] I. Souza, N. Marzari, and D. Vanderbilt, Maximally localized Wannier functions for entangled energy bands, Phys. Rev. B **65,** 035109 (2001).

[66] M. Pourfath, *The Non-Equilibrium Green's Function Method for Nanoscale Device Simulation* (Springer-Verlag, Wien, 2014).

[67] N. W. Ashcroft and N. D. Mermin, *Solid State Physics* (Saunders College Publishing, Orlando, 1976).

[68] S. Datta, *Electronic Transport in Mesoscopic Systems* (Cambridge University Press, Cambridge, 1995).

[69] S.-D. Liang, *Quantum Tunneling and Field Electron Emission Theories* (World Scientific, Singapore, 2012).

[70] T. Low, S. Hong, J. Appenzeller, S. Datta, and M. S. Lundstrom, Conductance asymmetry of graphene p-n junction, IEEE Trans. Electron Devices **56,** 1292 (2009).

[71] S. Wang, C. Ren, Y. Li, H. Tian, W. Lu, and M. Sun, Spin and valley filter across line defect in silicene, Appl. Phys. Express **11,** 053004 (2018).

[72] C. H. Lewenkopf and E. R. Mucciolo, The recursive Green's function method for graphene, J. Comput. Electron. **12,** 203 (2013).

[73] F. de Brito Mota, R. Rivelino, P. V. C. Medeiros, and C. M. C. de Castilho, A critical assessment on the electron transport through dehydrogenated intrinsically conducting channels in graphane-graphene hybrids, Mater. Res. Express **6,** 085618 (2019).

[74] W.-W. Tao, B. Liu, Q. Dai, and S.-K. Wang, Simulation of electronic total-reflection effect in a graphene junction, Commun. Theor. Phys. **61,** 391 (2014).

[75] S. K. Wang, J. Wang, and K. S. Chan, Multiple topological interface states in silicene, New J. Phys. **16,** 045015 (2014).

[76] K. Wakabayashi and T. Aoki, Electrical conductance of zigzag nanographite ribbons with locally applied gate voltage, Int. J. Mod. Phys. B **16,** 4897 (2002).

[77] C. D. Ren, W. T. Lu, B. H. Zhou, Y. F. Li, D. Y. Li, S. K. Wang, and H. Y. Tian, Controllable valley filter in graphene topological line defect with magnetic field, J. Phys.: Condens. Matter **32,** 365302 (2020).

[78] S.-K. Wang, J. Wang, and J.-F. Liu, Topological phase in one-dimensional Rashba wire, Chin. Phys. B **25,** 077305 (2016).

[79] J. J. Wang, S. Liu, J. Wang, and J.-F. Liu, Valley-coupled transport in graphene with Y-shaped Kekulé structure, Phys. Rev. B **98,** 195436 (2018).

[80] H. Haug and A.-P. Jauho, *Quantum Kinetics in Transport and Optics of Semiconductors* (Springer-Verlag, Berlin, 2008).

[81] A. R. Dmitry, *Theory of Quantum Transport at Nanoscale: An Introduction* (Springer International Publishing, Cham, 2015).

[82] M. P. Lopez Sancho, J. M. Lopez Sancho, and J. Rubio, Quick iterative scheme for the calculation of transfer matrices: application to Mo (100), J. Phys. F: Met. Phys. **14,** 1205 (1984).

[83] A. R. Akhmerov, J. H. Bardarson, A. Rycerz, and C. W. J. Beenakker, Theory of the valley-valve effect in graphene nanoribbons, Phys. Rev. B **77,** 205416 (2008).

[84] A. Cresti, G. Grosso, and G. P. Parravicini, Valley-valve effect and even-odd chain parity in p–n graphene junctions, Phys. Rev. B **77,** 233402 (2008).

[85] T. G. Pedersen and J. G. Pedersen, Self-consistent tight-binding model of B and N doping in graphene, Phys. Rev. B **87,** 155433 (2013).

[86] M. Büttiker, Y. Imry, R. Landauer, and S. Pinhas, Generalized many-channel conductance formula with application to small rings, Phys. Rev. B **31,** 6207 (1985).

[87] J. C. Cuevas and E. Scheer, *Molecular Electronics: An Introduction to Theory and Experiment* (World Scientific, Singapore, 2010).

[88] M. Seel and R. Pandey, Electronic and quantum transport properties of a graphene-BN dot-ring heteronanostructure, J. Phys. Commun. **2,** 045003 (2018).

[89] H. Tian, S. Wang, J. Hu, and J. Wang, The chirality dependent spin filter design in the graphene-like junction, J. Phys.: Condens. Matter **27,** 125005 (2015).

[90] H. Y. Tian, K. S. Chan, and J. Wang, Efficient spin injection in graphene using electron optics, Phys. Rev. B **86,** 245413 (2012).

[91] Y. Xing, J. Wang, and Q.-f. Sun, Focusing of electron flow in a bipolar graphene ribbon with different chiralities, Phys. Rev. B **81,** 165425 (2010).

[92] K. Michaeli, D. N. Beratan, D. H. Waldeck, and R. Naaman, Voltage-induced long-range coherent electron transfer through organic molecules, Proc. Natl. Acad. Sci. USA **116,** 5931 (2019).

[93] T. Ihn, *Semiconductor Nanostructures: Quantum States and Electronic Transport* (Oxford University Press, Oxford, 2009).

[94] F. Ma, Z. Guo, K. Xu, and P. K. Chu, First-principle study of energy band structure of armchair graphene nanoribbons, Solid State Commun. **152,** 1089 (2012).

[95] R. Saito, G. Dresselhaus, and M. S. Dresselhaus, *Physical Properties of Carbon Nanotubes* (Imperial College Press, London, 1998).

[96] S. Tiwari, *Nanoscale Device Physics: Science and Engineering Fundamentals* (Oxford University Press, New York, 2017).

[97] Y. J. Zhang, T. Oka, R. Suzuki, J. T. Ye, and Y. Iwasa, Electrically switchable chiral light-emitting transistor, Science **344,** 725 (2014).

[98] S. Wang, M. S. Ukhtary, and R. Saito, Strain effect on circularly polarized electroluminescence in transition metal dichalcogenides, Phys. Rev. Res. **2,** 033340 (2020).

[99] S. M. Sze and K. K. Ng, *Physics of Semiconductor Devices* (John Wiley & Sons, Hoboken, 2006).

[100] J. Wang, X. Chen, B.-F. Zhu, and S.-C. Zhang, Topological p-n junction, Phys. Rev. B **85,** 235131 (2012).

[101] L. Esaki, New phenomenon in narrow germanium p–n junctions, Phys. Rev. **109,** 603 (1958).

[102] V. V. Cheianov and V. I. Fal'ko, Selective transmission of Dirac electrons and ballistic magnetoresistance of

n–p junctions in graphene, Phys. Rev. B **74**, 041403(R) (2006).

[103] C. W. J. Beenakker, Colloquium: Andreev reflection and Klein tunneling in graphene, Rev. Mod. Phys. **80**, 1337 (2008).

[104] S. Das Sarma, S. Adam, E. H. Hwang, and E. Rossi, Electronic transport in two-dimensional graphene, Rev. Mod. Phys. **83**, 407 (2011).

[105] F. A. Chaves, P. C. Feijoo, and D. Jiménez, 2D pn junctions driven out-of-equilibrium, Nanoscale Adv. **2**, 3252 (2020).

[106] D. Reuter, C. Werner, A. D. Wieck, and S. Petrosyan, Depletion characteristics of two-dimensional lateral p–n-junctions, Appl. Phys. Lett. **86**, 162110 (2005).

[107] F. Wu, Q. Li, P. Wang, H. Xia, Z. Wang, Y. Wang, M. Luo, L. Chen, F. Chen, J. Miao, X. Chen, W. Lu, C. Shan, A. Pan, X. Wu, W. Ren, D. Jariwala, and W. Hu, High efficiency and fast van der Waals hetero-photodiodes with a unilateral depletion region, Nat. Commun. **10**, 4663 (2019).

[108] A. Nipane, S. Jayanti, A. Borah, and J. T. Teherani, Electrostatics of lateral p-n junctions in atomically thin materials, J. Appl. Phys. **122**, 194501 (2017).

[109] H.-K. Lyeo, A. A. Khajetoorians, L. Shi, K. P. Pipe, R. J. Ram, A. Shakouri, and C. K. Shih, Profiling the thermoelectric power of semiconductor junctions with nanometer resolution, Science **303**, 816 (2004).

[110] J. A. Blackburn, *Modern Instrumentation for Scientists and Engineers* (Springer-Verlag, New York, 2001).

[111] G. Rockis, *Solid State Fundamentals* (American Technical Publishers, Chicago, 2001).

[112] E. Ramshaw, *Power Electronics Semiconductor Switches* (Springer, Boston, 1993).

[113] B. K. Ridley, Specific negative resistance in solids, Proc. Phys. Soc. **82**, 954 (1963).

[114] S. Piscanec, M. Lazzeri, F. Mauri, and A. C. Ferrari, Optical phonons of graphene and nanotubes, Eur. Phys. J. Spec. Top. **148**, 159 (2007).

[115] R. Murali, *Graphene Nanoelectronics: From Materials to Circuits* (Springer-Verlag, New York, 2012).

[116] J.-H. Chen, C. Jang, S. Xiao, M. Ishigami, and M. S. Fuhrer, Intrinsic and extrinsic performance limits of graphene devices on SiO_2, Nat. Nanotechnol. **3**, 206 (2008).

[117] F. Cervantes-Sodi, G. Csányi, S. Piscanec, and A. C. Ferrari, Edge-functionalized and substitutionally doped graphene nanoribbons: Electronic and spin properties, Phys. Rev. B **77**, 165427 (2008).

[118] F. López-Urías, J. L. Fajardo-Díaz, A. J. Cortés-López, C. L. Rodríguez-Corvera, L. E. Jiménez-Ramírez, and E. Muñoz-Sandoval, Understanding the electrochemistry of armchair graphene nanoribbons containing nitrogen and oxygen functional groups: DFT calculations, Phys. Chem. Chem. Phys. **22**, 4533 (2020).